



Sulfamethoxazole degradation via peroxydisulfate activation over WO₃/MIL-100(Fe) under low power LED visible light

Ke-Xin Shi^a, Fuguo Qiu^{a,b}, Jia-Wei Wang^a, Peng Wang^a, Hai-Yan Li^{b,c}, Chong-Chen Wang^{a,b,c,*}

^a Beijing Key Laboratory of Functional Materials for Building Structure and Environment Remediation, School of Environment and Energy Engineering, Beijing University of Civil Engineering and Architecture, Beijing 100044, China

^b Beijing Energy Conservation & Sustainable Urban and Rural Development Provincial and Ministry Co-construction Collaboration Innovation Center, Beijing University of Civil Engineering and Architecture, Beijing 100044, China

^c Beijing Engineering Research Center of Sustainable Urban Sewage System Construction and Risk Control, Beijing University of Civil Engineering and Architecture, Beijing 100044, China

ARTICLE INFO

Keywords:

MIL-100(Fe)
WO₃
Sulfamethoxazole
Peroxydisulfate
Z-Scheme

ABSTRACT

Series of WO₃/MIL-100(Fe) (WxMy) composites were synthesized via the mild solvent evaporation method, which were used as a heterogeneous sulfate radical-advanced oxidation process (SR-AOP) catalyst for sulfamethoxazole (SMX) degradation. The as-prepared W4M1 (0.25 g/L) demonstrated excellent SR-AOP catalysis activity with 100 % SMX (5 mg/L) degradation efficiency within 15 min under visible light. The influences of initial pH, peroxydisulfate (PDS) concentration, catalyst dosage, and inorganic anions as well as the degradation pathway were investigated. The effective transfer of the photo-generated electrons from WO₃ to MIL-100(Fe) via Z-scheme mechanism contributed to the outstanding SR-AOP catalysis activity of W4M1, which were affirmed by both the active species capture experiments and electron spin resonance (ESR) experiments. Moreover, W4M1 displayed excellent stability and reusability throughout five runs' cycling experiments. This work offered a new SR-AOP catalyst alteration to eliminate emerging pollutant under visible light, which might provide insight clue for catalyst design and fabrication.

1. Introduction

Sulfonamide antibiotics (SAs), as a major class of anti-microbial drugs, are broadly resistant to both Gram-positive and Gram-negative bacteria [1], which are frequently detected in different water environments [2,3]. Although current research indicates that sulphonamide antibiotics are not highly toxic to vertebrates, they still pose a significant potential threat to natural ecosystems and human health [4]. As one of the SAs, sulfamethoxazole (SMX) has been listed as one of the 30 most common wastewater pollutants by the U.S. Geological Survey, with a half-life of 85–100 days or more [5]. It is essential to eliminate the potential threat of sulphonamide antibiotics.

Advanced oxidation processes (AOPs) have been adopted widely as an effective method for water treatment [6–8]. In recent years, the sulfate radicals-advanced oxidation processes (SR-AOP) have attracted increasing interest, in which the •SO₄⁻ is usually produced by peroxymonosulfate (PMS) and peroxydisulfate (PDS) activation in the

presence of light, heat, ultrasound, and catalysts [9,10].

Nowadays, the increasing attentions are paid to develop or explore the heterogeneous catalysts to degrade various organic pollutants [11–13]. The porous metal–organic frameworks (MOFs) arose widespread interest due to their special characterizations like ultra-high surface areas, tunable crystalline structures and porous sizes [14–18]. MIL-100(Fe) as an iron-based catalyst shows the high specific surface area, thermal stability, water stability and good catalytic activity, which can be potentially used to activate persulfates [19]. There are many previous examples of MIL-100(Fe) for persulfates activation to achieve organic pollutants degradation. In our group, Zhao et al. [19] prepared Bi₁₂O₁₇Cl₂/MIL-100(Fe) composites to accomplish the Cr(VI) reaction under visible light and BPA degradation in the presence of both PDS and visible light. Up to now, the individual WO₃ was used to photoactivate persulfate due to its outstanding photocatalysis activity [20,21]. Although several cases about construction of heterojunction between WO₃ and MIL series MOF were reported [22,23], to the best of our

* Corresponding author at: Beijing Key Laboratory of Functional Materials for Building Structure and Environment Remediation, School of Environment and Energy Engineering, Beijing University of Civil Engineering and Architecture, Beijing 100044, China.

E-mail address: wangchongchen@bucea.edu.cn (C.-C. Wang).

<https://doi.org/10.1016/j.seppur.2022.122991>

Received 4 October 2022; Received in revised form 18 December 2022; Accepted 20 December 2022

Available online 23 December 2022

1383-5866/© 2022 Elsevier B.V. All rights reserved.

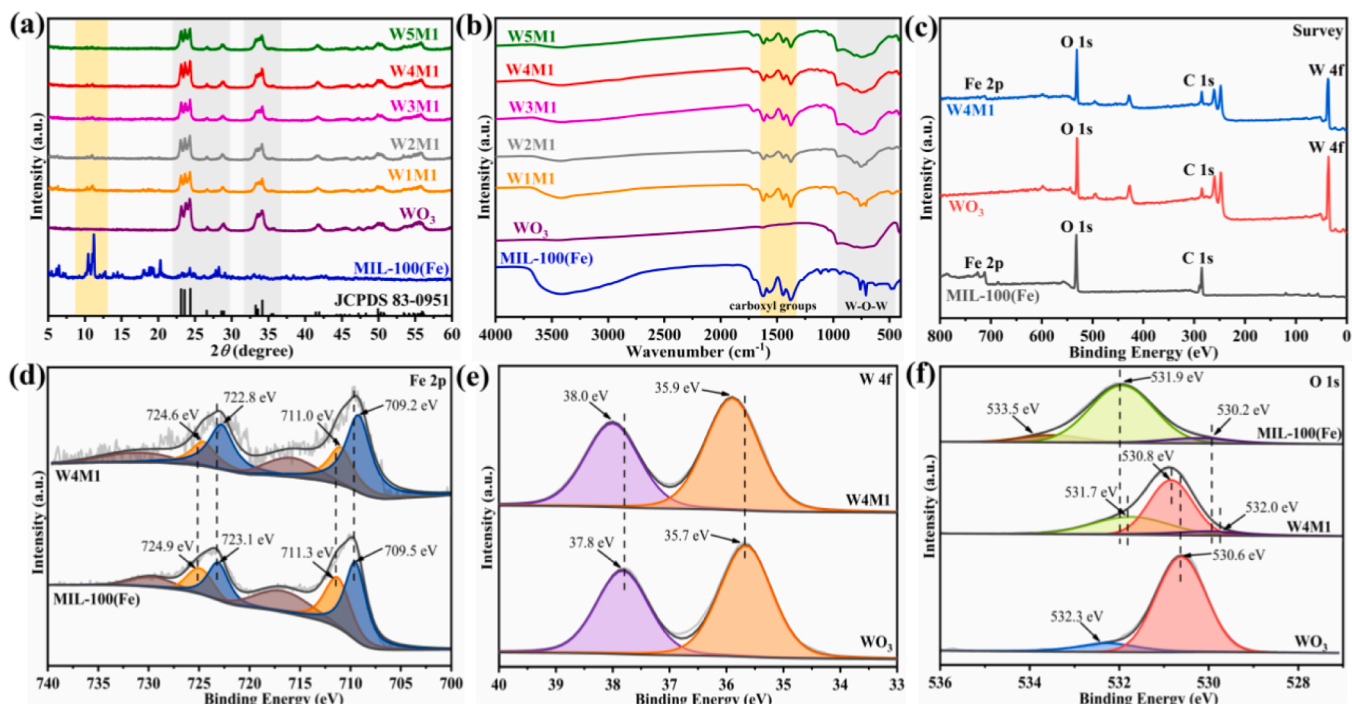


Fig. 1. (a) The PXRD patterns and (b) FTIR spectra of the individual MIL-100(Fe), WO_3 , and W_xM_y composites. (c) The XPS survey spectra and the high-resolution XPS spectra of (d) Fe 2p, (e) W 4f and (f) O 1s for MIL-100(Fe), WO_3 , and W4M1 composite.

knowledge, there is no research about WO_3/MOF composites for PDS activation.

Inspired by our previous work, within this paper, WO_3 nanoplate and MIL-100(Fe) octahedron were adopted to fabricate $\text{WO}_3/\text{MIL-100(Fe)}$ composites via a mild solvent evaporation method for the purpose of accomplishing effective SMX degradation by SR-AOP. Both the influences of initial pH, PDS dosage, co-existing ions and degradation pathway of SMX were investigated and clarified. Finally, a mechanism for the PDS activation over the $\text{WO}_3/\text{MIL-100(Fe)}$ to degrade SMX was proposed and validated.

2. Experimental

The used chemicals, the instruments and the corresponding methods were provided in the [Supplementary Information](#).

2.1. Fabrication $\text{WO}_3/\text{MIL-100(Fe)}$ composites

WO_3 nanoplate and MIL-100(Fe) octahedron were synthesized according to the literatures, respectively [24,25]. The details on synthesis were available in the [Supplementary Information](#).

$\text{WO}_3/\text{MIL-100(Fe)}$ composites were produced by a mild solvent evaporation method. Briefly, a certain amount of WO_3 nanoplate and MIL-100(Fe) octahedron were dispersed in 80.0 mL methanol by being sonicated for 15.0 min. Subsequently, the mixed solution was stirred until all the liquid evaporated, and the samples were dried in an oven at 60 °C. The $\text{WO}_3/\text{MIL-100(Fe)}$ composites were obtained by drying the evaporated sample in an oven at 60 °C for 12 h, which were named as W_xM_y (W and M represent WO_3 nanoplate and MIL-100(Fe) octahedron, x and y represent the mass fraction of WO_3 and MIL-100(Fe), respectively). The total amount of WO_3 and MIL-100(Fe) was 200.0 mg.

2.2. SR-AOP performance test

20.0 mg W_xM_y catalyst was mixed into 80.0 mL aqueous solution containing 5.0 mg/L SMX to accomplish adsorption-desorption

equilibrium in dark. After that, the suspension was irradiated under 25 W low power LED light (Beijing Aulight Co., Ltd., the light source spectrum showed in [Fig. S1](#)) to induce the SR-AOP for SMX degradation. The residual SMX concentration was determined by liquid chromatography (LC-20A) equipping with a 270 nm UV detector and Eclipse Plus C18 column. The other information was listed in [Supplementary Information](#).

3. Results and discussion

3.1. Characterizations

The powder X-ray diffraction (PXRD) patterns for MIL-100(Fe), WO_3 , and W_xM_y composites were shown in [Fig. 1a](#). The characteristic peaks of WO_3 were found at $2\theta = 23.1^\circ$, 23.6° and 24.4° , which correspond to (002), (020) and (200) planes of the crystal structure of WO_3 (JCPDS no. 83-0951). According to the previous reports, the exposed facets of (002), (020), and (200) of WO_3 were reported to display high reactivity [26–30]. Meanwhile, the main characteristic peaks of the as-prepared MIL-100(Fe) at 6.2° , 10.2° , 11.0° , 20.0° were in agreement with the MIL-100(Fe) reported in previous literature [31]. As for the W_xM_y , the characteristic peaks of both WO_3 and MIL-100(Fe) were observed. Moreover, with increasing amounts of WO_3 in W_xM_y , the peaks of the MIL-100(Fe) gradually decreased, which was related to both the cover of WO_3 and the relatively low intensity of the MIL-100(Fe) [32].

Fourier transform infrared spectra (FTIR) of the synthesized materials were presented in [Fig. 1b](#). The peak at 712 cm^{-1} is ascribed to stretching of benzene ring [33]. The characteristic peaks observed at 1614 cm^{-1} , 1574 cm^{-1} , 1452 cm^{-1} , and 1385 cm^{-1} could be regarded as the characteristic peaks of the carboxyl group [34]. According to previous literature, the peaks in the range of $450\text{--}900\text{ cm}^{-1}$ were attributed to the W-O-W stretching vibrations [35]. The observed FTIR spectra of as-prepared catalysts confirmed the formation of W_xM_y composites.

The XPS (X-ray photoelectron spectroscopy) measurement was applied to test the elemental composition and binding position of MIL-

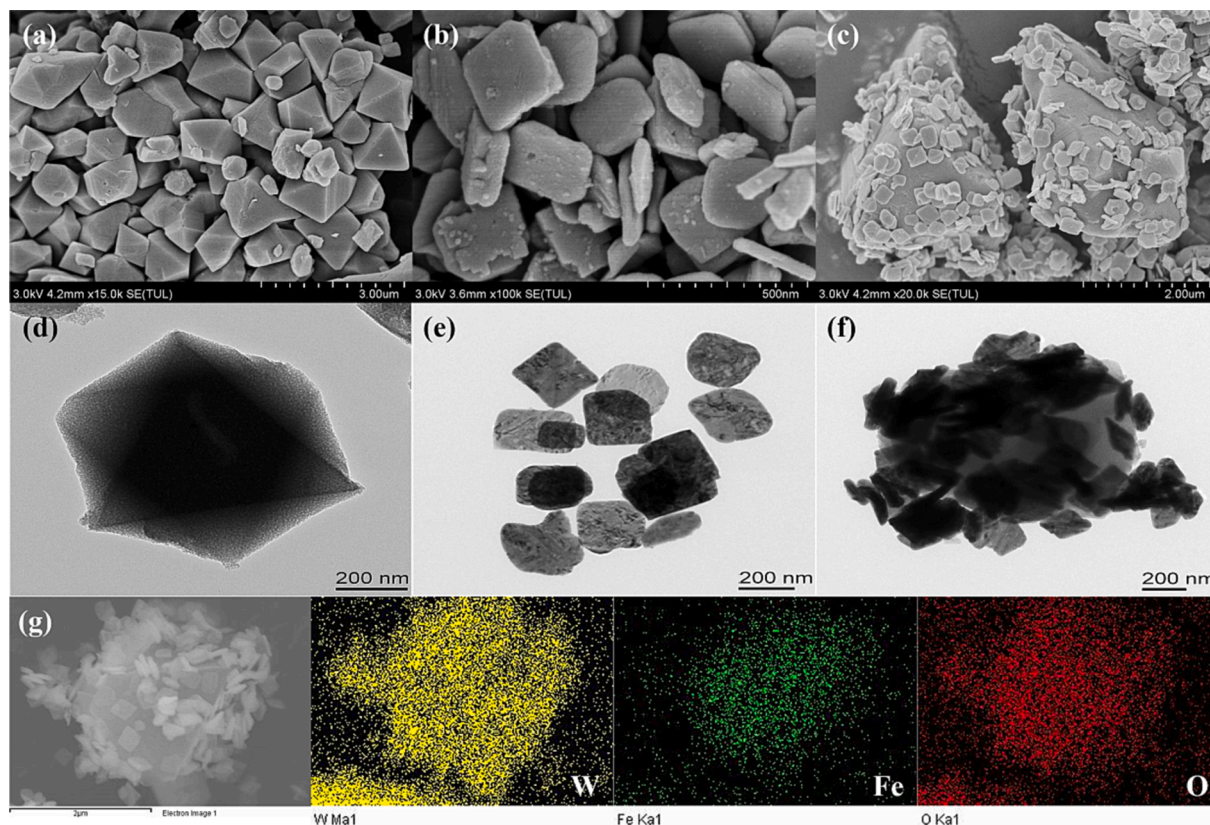


Fig. 2. The SEM and TEM images of (a, d) MIL-100(Fe), (b, e) WO_3 and (c, f) W4M1 composite. (g) The EDS elemental mappings of the W4M1 composite.

100(Fe), WO_3 , and W4M1. As shown in Fig. 1c, the XPS survey spectrum of W4M1 displayed characteristic peaks of Fe, C, O, and W, demonstrating the presence of MIL-100(Fe) and WO_3 . After being composited by solvent evaporation method, it was obvious that the Fe 2p peaks were shifted from 709.5 and 723.1 eV for Fe^{2+} along with 711.3 and 724.9 eV for Fe^{3+} in MIL-100(Fe) [8,36] to 709.2 and 722.8 eV for Fe^{2+} along with 711.0 and 724.6 eV for Fe^{3+} in W4M1 (Fig. 1d). While the peaks of W 4f were shifted from 35.7 and 37.8 eV for W^{6+} in WO_3 [37] to 35.9 and 38.0 eV in W4M1 (Fig. 1e). The blue shift of the Fe 2p peaks and red shift of the W 4f peaks implied that electrons were possibly transferred from WO_3 to MIL-100(Fe) [38]. The O1s spectrum for WO_3 (Fig. 1f) displayed peaks at 530.6 and 532.3 eV were attributed to the lattice oxygen (W-O) and hydroxyl oxygen, respectively [39]. The peaks at 530.2, 531.9, and 533.5 eV in MIL-100(Fe) attributed to Fe-O bonds, carboxyl groups and the adsorbed water molecules, respectively [34,40]. The O1s peaks of WO_3 shifted towards higher binding energy while that of MIL-100(Fe) shifted towards lower binding energy to form W4M1 composite.

The SEM and TEM images were conducted to deeply investigate the morphologies of MIL-100(Fe), WO_3 , and W4M1 (Fig. 2a–2f). It showed that the MIL-100(Fe) is comprised of octahedral microcrystals with an edge length of 2–3 μm (Fig. 2a and 2d). The WO_3 had a diameter size of 200–400 nm with a plate morphology, significantly smaller than that of MIL-100(Fe) (Fig. 2b). The plates of the WO_3 morphology were also confirmed by TEM observations (Fig. 2e). The morphology of the W4M1 composite was shown in Fig. 2c and 2f, revealing that WO_3 were closely anchored on the surface of MIL-100(Fe). Additionally, MIL-100(Fe) maintained the regular octahedron morphology after solvent evaporation of the composites, indicating that the MIL-100(Fe) structure was maintained in the solvent evaporation treatment process of composites. The successful fabrication of W4M1 was affirmed by EDS elemental mappings in Fig. 2g. It proved that the Fe element in MIL-100(Fe) and the W element in WO_3 were evenly distributed over the W4M1

composite. The high-resolution transmission electron microscope (HRTEM) image of W4M1 (Fig. S2) demonstrated the distinct and tight interface between WO_3 and MIL-100(Fe), in which the lattice fringe of 0.377 nm could be assigned to the (020) facets of WO_3 (JCPDS no. 83–0951).

The UV–vis DRS of MIL-100(Fe), WO_3 , and WxMy (Fig. 3a) displayed that all materials exhibited visible light absorption property. The band gaps of MIL-100(Fe) and WO_3 was calculated to be 2.61 eV [41] and 2.75 eV [42], respectively (Fig. 3b). The declining band gaps of composites could facilitate the superior visible-light response to individual WO_3 and MIL-100(Fe), contributing to the boosted SR-AOP performance.

The Mott-Schottky plots of the individual MIL-100(Fe) and WO_3 were shown in Fig. 3c and 3d, in which the positive slopes of the plots revealed an n-type semiconductor feature for the prepared samples [32,43]. The flat band potential (E_{FB}) for MIL-100(Fe) and WO_3 were about -0.43 eV vs. Ag/AgCl (-0.23 eV vs. NHE) and -0.17 eV vs. Ag/AgCl ($+0.03$ eV vs. NHE), respectively. For n-type semiconductors, the E_{FB} was located ca. 0.1 eV above the E_{CB} [44]. The E_{LUMO} of MIL-100(Fe) and the E_{CB} of WO_3 were calculated to be about -0.33 eV and -0.07 eV (vs. NHE), respectively. Combined with the value of E_g , the E_{HOMO} of MIL-100(Fe) and the E_{VB} of WO_3 were 2.28 eV and 2.68 eV vs. NHE, respectively.

The X-ray fluorescence (XRF) characterization technique was utilized to explore the W and Fe contents in the W4M1 composite. The ratio of WO_3 and MIL-100(Fe) in W4M1 can be calculated as 4.8:1 based on the XRF results of W (93.124 %) and Fe (6.234 %) weight percentage (Table S1).

The N_2 adsorption–desorption isotherms and the pore size distribution of the WO_3 , MIL-100(Fe) and WxMy were exhibited in Fig. S3. MIL-100(Fe) and WxMy displayed the type I isotherms based on IUPAC, which can be attributed to the microporous characteristics. The surface area, average pore size and total pore volume were shown in Table S2.

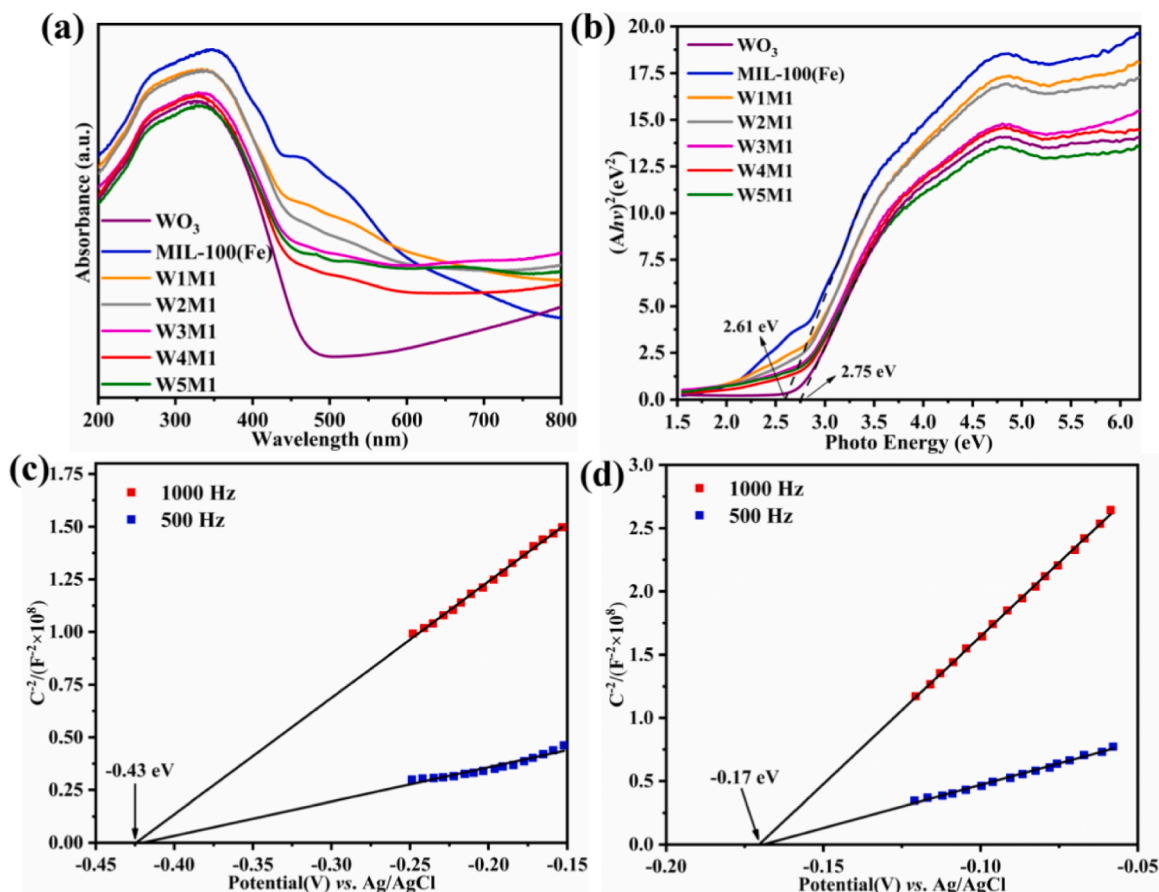


Fig. 3. (a) The UV-vis DRS and (b) the E_g plots of the MIL-100(Fe) octahedron, WO_3 nanoplate and W_xM_y catalysts. Mott-Schottky plots of (c) MIL-100(Fe) octahedron and (d) WO_3 nanoplate at different frequencies.

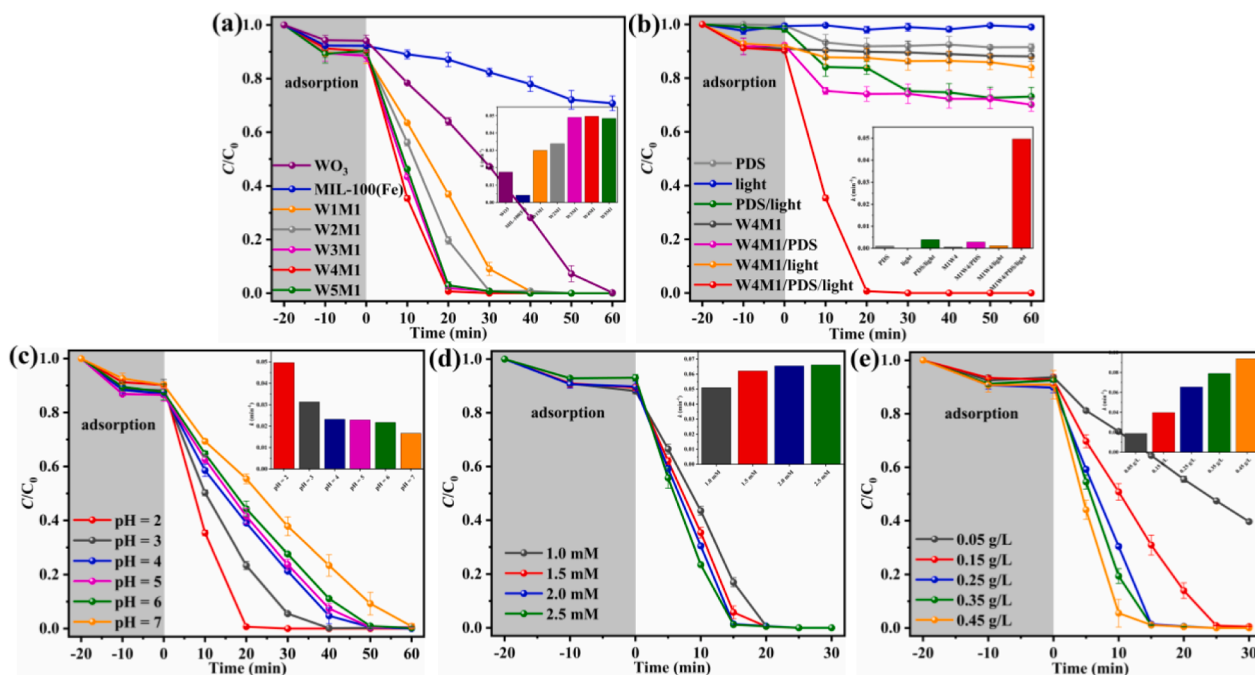


Fig. 4. (a) The SMX degradation efficiencies over different catalysts via SR-AOP under visible light. (b) The SMX degradation efficiencies in different systems. The influences of (c) initial pH, (d) PDS concentration and (e) catalysis dosage on SMX degradation over W4M1. Experimental conditions: catalysts dosage = 0.25 g/L (except Fig. 4e), [PDS] = 1.5 mM (for Fig. 4a, b and c) and 2.0 mM (for Fig. 4e), [SMX] = 5 mg/L, volume = 80 mL and pH = 2.0 (except Fig. 4c).

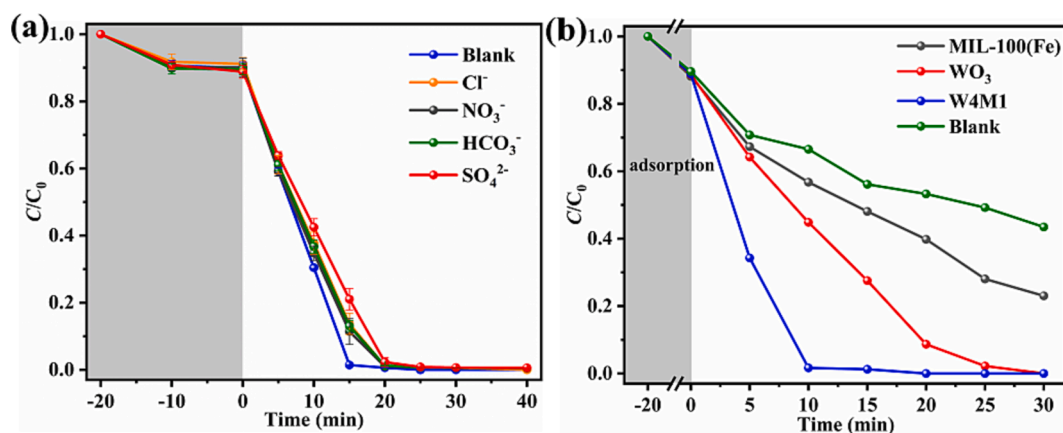


Fig. 5. (a) Inorganic ions on SMX degradation over W4M1. (b) The photo-activated SR-AOP of SMX degradation under real solar irradiation. Experimental conditions: catalyst dosage = 0.25 g/L, [PDS] = 2.0 mM, [SMX] = 5 mg/L, volume = 80 mL, pH = 2.0 and inorganic anions = 1.0 mM.

Compared to MIL-100(Fe), WO_3 displayed low specific surface. As the percentage of MIL-100(Fe) in the composites increased, the specific surface area and total pore volume progressively increased. Hence, more active sites could be provided to facilitate the diffuse of target pollutants within the porous structure for improved catalytic ability [45].

3.2. Photoactivated SR-AOP toward SMX degradation

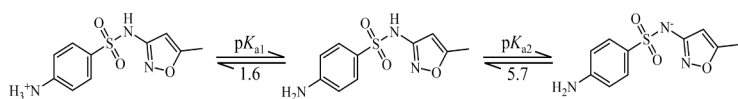
The performance of MIL-100(Fe) octahedron, WO_3 nanoplate, and WxMy composites in activating PDS to degrade SMX were evaluated in Fig. 4a. A dark experiment was carried out for adsorption-desorption equilibrium to explore the adsorption influence. The initial adsorption efficiencies of SMX by MIL-100(Fe), WO_3 , and WxMy were limited (<12 %). Both individual MIL-100(Fe) and WO_3 exhibited poor ability to activate PDS under visible light. All WxMy composites exhibited a superior performance to individual MIL-100(Fe) and WO_3 . With different contents of WO_3 in W1M1, W2M1, W3M1, W4M1 and W5M1, the degradation efficiency increased to ca. 91.0 %, 99.2 %, 99.2 %, 100 %, and 99.3 % within 30 min, which was ascribed to the redshift of visible light absorption and the formed heterojunction structure. Among these composites, W4M1 exhibited the best photoactivated SR-AOP performance, in which the SMX decomposition efficiency increased to 99.3 % at 20 min. The removal rate of SMX was accordance with zero-order reaction kinetics (Table S3-S7), the apparent reaction kinetic constant of SMX degradation reaction for W4M1 was calculated as 0.04963 min^{-1} .

The synergistic effects of W4M1 catalyst and visible light on PDS activation for SMX degradation were assessed (Fig. 4b). Without PDS, the visible light irradiation did not result in any SMX degradation. The W4M1 exhibited the limited adsorption toward SMX. Significantly, almost complete SMX removal (99.3 %) was accomplished in 20 min

60 min. The W4M1/PDS/light showed higher degradation efficiency than the sum of the efficiencies of the individual PDS, light, W4M1 adsorption, PDS/light, W4M1/PDS, and W4M1/light process, demonstrating the synergistic effects of light and W4M1 on PDS activation.

3.3. The influences factors on SMX degradation

The influences of initial pH, PDS concentrations and catalyst dosage on SMX degradation were shown in Fig. 4c-4f. Finally, we carried out subsequent experiments at the conditions of pH = 2.0, 2 mM PDS and 0.25 g/L catalyst. Moreover, the k value of SMX degradation reaction under the optimum condition was calculated as 0.06545 min^{-1} . To test the stability of W4M1 under different pH conditions, the leaching Fe and W ions (Fig. S4) as well as PXRD patterns of the used W4M1 after reaction at different pHs (Fig. S5) were tested. The corresponding results confirmed that W4M1 was stable with low Fe and W leaching as well as well-maintained morphology. To examine the role of the leaching Fe and W ions from W4M1 at different pHs, the dissolved Fe^{2+} and W^{6+} with the identical concentrations to the leached ones from W4M1 were used to perform the homogeneous SR-AOP reaction. Under each pH condition, SMX was slightly degraded in the simulated homogeneous SR-AOP reaction (Fig. S6), suggesting that the homogeneous SR-AOP reaction did not make major contribution. Furthermore, the zeta potentials of WO_3 , MIL-100(Fe) and W4M1 were measured. As shown in Fig. S7, the surface of W4M1 was negatively charged at pH 2.0–7.0. The pK_{a1} (1.6) and pK_{a2} (5.7) values of SMX along with the speciation were expressed in the Eq. (1) [46]. The SMX molecules were neutral or negatively charged at pH values between 2.0 and 7.0. Hence, no noticeable electrostatic attraction was presented between W4M1 and SMX.



through the joint action of visible light, W4M1 and PDS. Moreover, control experiments of PDS/light, W4M1/PDS and W4M1/light systems were also performed. The individual W4M1 achieved a limited degradation of SMX via photocatalysis (W4M1/light system), and visible light activated PDS had a limited SMX removal efficiency (PDS/light system). Moreover, compared to the W4M1/PDS/light process, W4M1 demonstrated much lower PDS activation with the SMX removal of 34.9 % in

Real water bodies contain a certain amount of co-existing ions [47,48]. Several inorganic anions (Cl^- , NO_3^- , HCO_3^- , and SO_4^{2-}) were deliberately introduced into the W4M1/PDS/light degradation system (Fig. 5a). Fortunately, all inorganic anions showed negligible inhibitory effects. Compared with blank experiment, the SMX removal ratio were almost kept unchanged with addition of Cl^- (1 mM) and NO_3^- (1 mM), respectively. It was reported that Cl^- can react with $\bullet SO_4$ to produce less

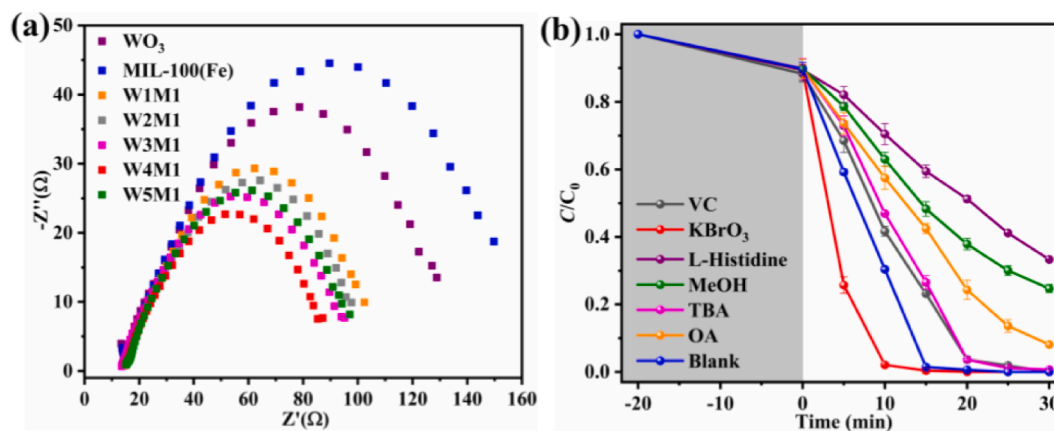
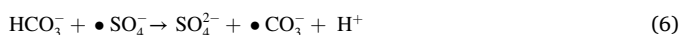
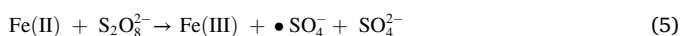
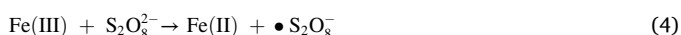
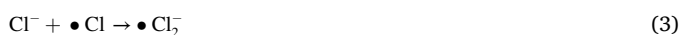


Fig. 6. (a) The EIS images of different used catalysts. (b) Capture experiment of SMX degradation over W4M1. Experimental conditions (for b): catalyst dosage = 0.25 g/L, [PDS] = 2.0 mM, [SMX] = 5 mg/L, volume = 80 mL, pH = 2.0.

reactive $\bullet\text{Cl}$ and $\bullet\text{Cl}_2$ anions. According to Eqs. (2) and (3), the redox potentials of $\bullet\text{Cl}$ (2.4 V) and $\bullet\text{Cl}_2$ (2.1 V) are lower than that of $\bullet\text{SO}_4$ (2.5–3.1 eV) [49,50]. It is deemed that NO_3^- could interact with the electrons to form NO_2 , which partially scavenges ROS [51]. The SO_4^{2-} exerted an inhibitory influence on the SMX degradation, because that SO_4^{2-} would hinder the forward reactions of Eqs. (4) and (5), resulting in $\bullet\text{SO}_4$ decreases and degradation efficiency decreases [52]. According to Eq. (6), HCO_3^- depression of SMX degradation efficiency was most effectively inhibited, due to that HCO_3^- can trap $\bullet\text{SO}_4$ to yield the less oxidative $\bullet\text{HCO}_3$ [53].



The solar light was used as the light source to further explore the potential of W4M1 for the practical SR-AOP process (Fig. 5b). According to the results from pure materials and blank experiment, the performance of W4M1 photo-activated SR-AOP in degrading SMX was significantly improved. Nearly complete removal of SMX was observed after 10 min.

The as-prepared W4M1 exhibit superior peroxydisulfate activation performance to the counterpart catalysts (Table S8). As well, some typical organic pollutants like bisphenol A (BPA), carbamazepine (CBZ),

ofloxacin (OFC), diclofenac (DCF) and atrazine (ATZ) were selected as degradation targets to further investigate the universal applicability of W4M1 (Fig. S8). All selected pollutants could be degraded within 60 min, indicating the excellent peroxydisulfate activation performance over W4M1 under visible light towards various organic pollutants. Thus, the W4M1 composite may have high application value in the field of SR-AOP process in the future.

3.4. Possible mechanisms

The electrochemical impedance spectroscopy (EIS) for WO₃, MIL-100(Fe) and WxMy were shown in Fig. 6a. The Nyquist radius of W4M1 was smaller than those of the other catalysts, suggesting that the W4M1 demonstrated a weaker charge transfer resistance and thus improved degradation performance [54].

To identify the major active species produced during the SR-AOP process, some capture experiments by different scavengers were performed. Typical scavengers, including oxalic acid (OA), potassium bromate (KBrO₃), ascorbic acid (VC), *tert*-butanol (TBA) and methanol (MeOH) were chosen as the quenchers of h^+ , e^- , $\bullet\text{O}_2$, $\bullet\text{OH}$ and $\bullet\text{SO}_4$, respectively [55–58]. As shown in Fig. 6b, the addition of MeOH caused obviously deactivation of SR-AOP process, indicating that $\bullet\text{SO}_4$ is a main active substance in the system towards SMX degradation [59]. The degradation rate decreased after adding OA, due to that h^+ can oxidize SMX directly and can also react with water in the system to form $\bullet\text{OH}$ to oxidize SMX [5]. By adding TBA for comparison, the remove efficiencies of SMX were slightly inhibited, indicating $\bullet\text{OH}$ was also one of the active substances in the system [60]. The SMX degradation efficiency had a slight inhibitory in the presence of VC, implying the $\bullet\text{O}_2$ played an

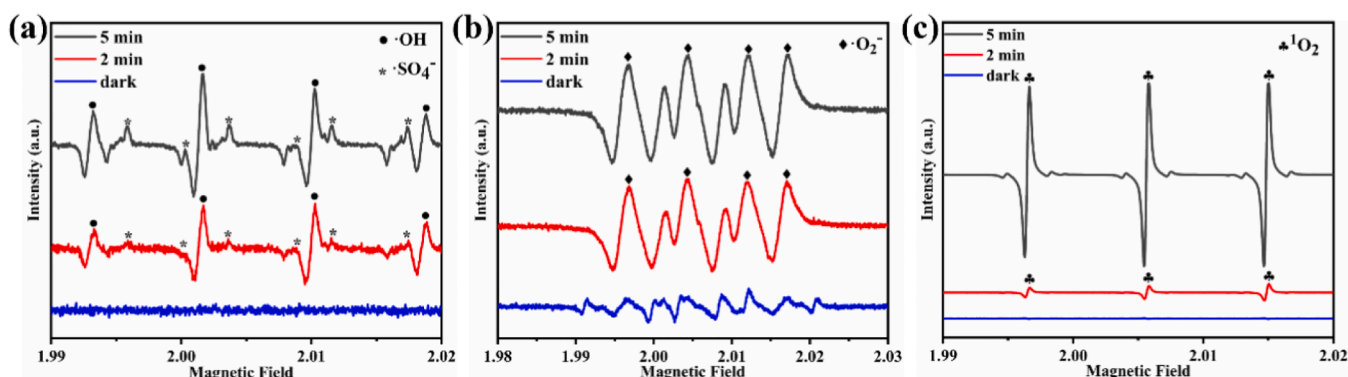


Fig. 7. ESR spectra of (a) $\bullet\text{OH}$, $\bullet\text{SO}_4$, (b) $\bullet\text{O}_2^-$, (c) $^1\text{O}_2$ radicals for W4M1.

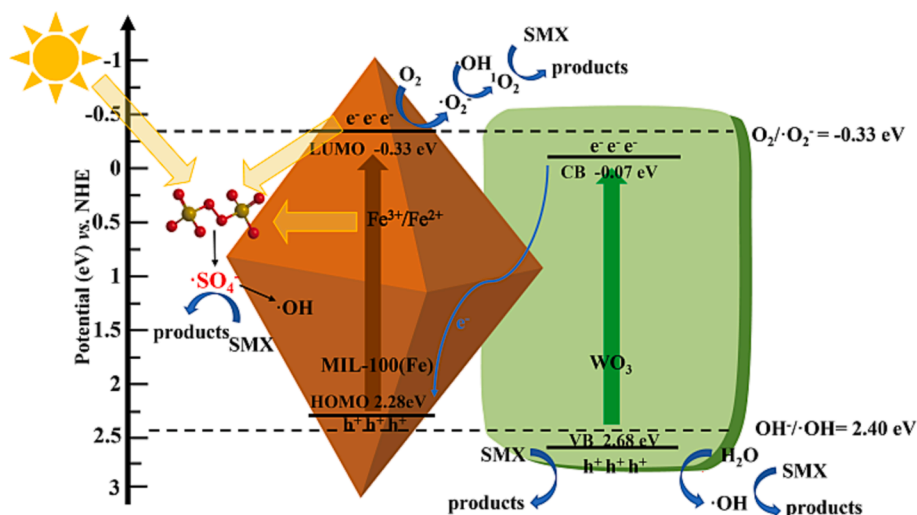


Fig. 8. The mechanism diagram of SMX degradation via PDS activation over W4M1.

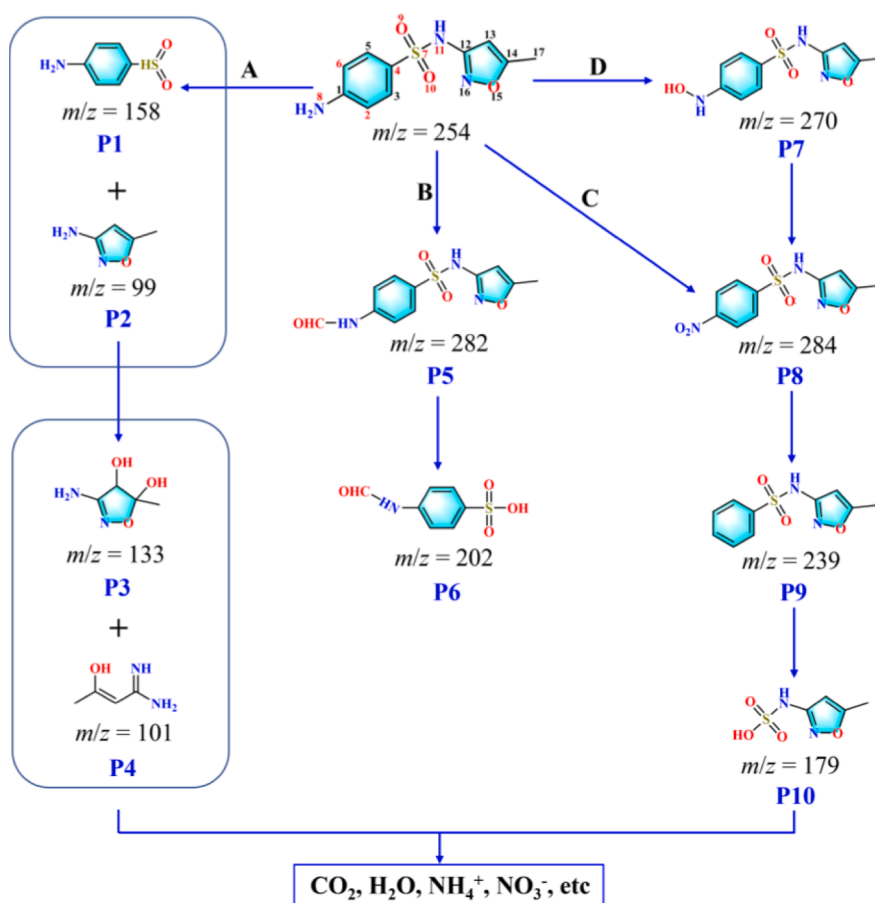


Fig. 9. Proposed SMX degradation pathways via peroxydisulfate activation over W4M1 under visible light.

insignificant role in SR-AOP system [61]. Conversely, the removal efficiency was increased by trapping e^- with $KBrO_3$. The introduction of $KBrO_3$ promoted the separation of holes and electrons, producing more holes which can increase the SMX degradation efficiency [62]. We also investigated the effect of non-radical reactive substances on SMX degradation by adding L-histidine to capture singlet oxygen (1O_2). It was noted that SMX degradation is significantly inhibited, implying 1O_2 was also involved in the degradation of SMX by W4M1 [63].

The electron spin resonance (ESR) experiments were conducted to identify the active substances that function in the W4M1/PDS/light system, in which both the characteristic signals of $DMPO \cdot SO_4^-$ and $DMPO \cdot OH$ with visible light irradiation and PDS of the W4M1 system (Fig. 7a), which meant that $\cdot SO_4^-$ and $\cdot OH$ were generated in the above systems. $DMPO \cdot O_2^-$ peaks could be observed in the studied system under visible light (Fig. 7b) to affirm the existence of $\cdot O_2^-$. The gradual increasing of the triplet peaks with relative intensities of 1:1:1 can be

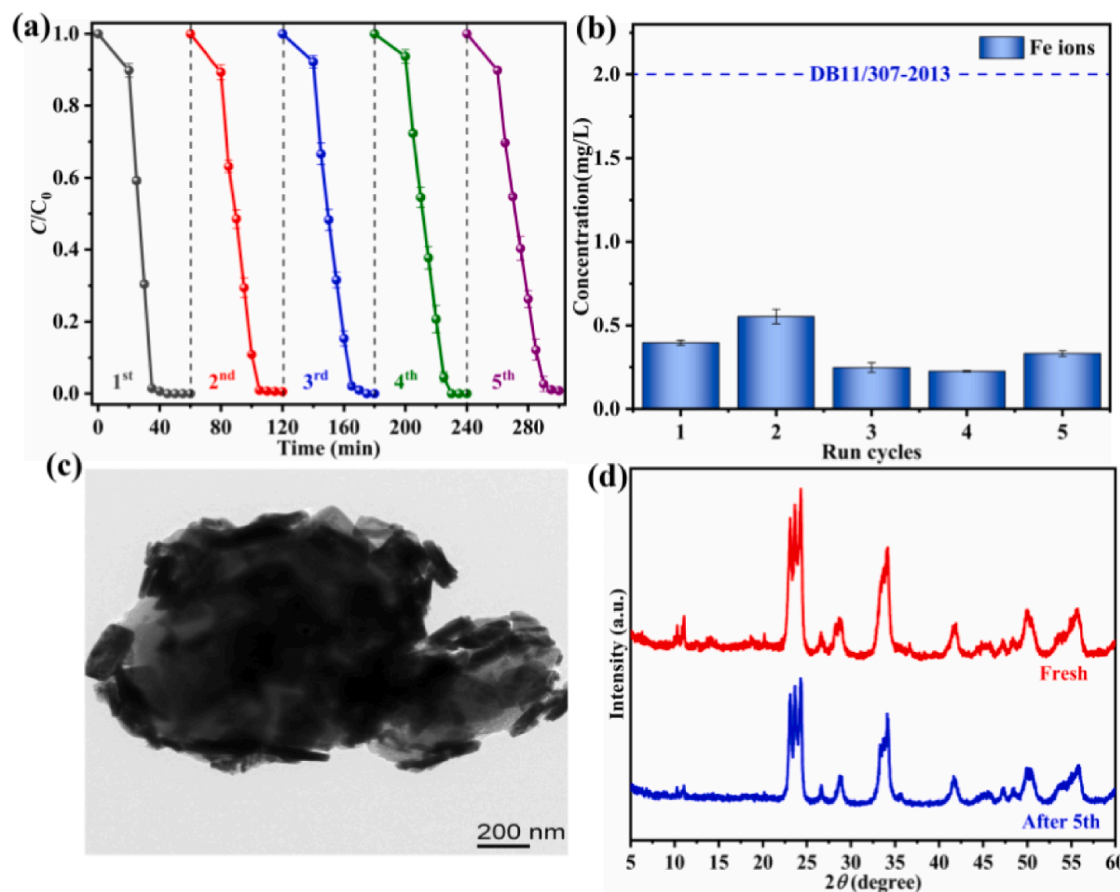


Fig. 10. (a) The cycle experiments of SMX degradation over W4M1, (b) Fe ion leaching during cycle experiments, (c) TEM image of W4M1 after cycle experiments and (d) PXRD patterns of W4M1 before and after cycle experiment. Experimental conditions (for a): catalyst dosage = 0.25 g/L, [PDS] = 2.0 mM, [SMX] = 5 mg/L, volume = 80 mL, pH = 2.0.

ascribed to the continuous $^1\text{O}_2$ generation with the prolonging visible light illumination time (Fig. 7c). To further validate the generation of $\bullet\text{SO}_4$ and $\bullet\text{OH}$ in the SR-AOP system under different pHs, the $\bullet\text{SO}_4$ and $\bullet\text{OH}$ concentrations and pH after reaction were measured [64,65]. The findings (Fig. S9) demonstrated that under different pH conditions, the SR-AOP system could produce $\bullet\text{SO}_4$ and $\bullet\text{OH}$ to degrade SMX.

Furthermore, the band structure of W4M1 was proposed to illustrate the possible degradation mechanism. Based on the above analysis, the O_2 could not combine with the photo-induced electrons on the CB of WO_3 to produce $\bullet\text{O}_2^-$ ($\text{O}_2/\bullet\text{O}_2^-$ with a standard potential of -0.33 eV vs. NHE). However, the W4M1 could produce $\bullet\text{O}_2^-$, implying that the photogenerated electrons and holes of W4M1 accumulated on the LUMO of MIL-100(Fe) and the VB of WO_3 , respectively. In other words, the photogenerated electrons on CB of WO_3 were transferred to the HOMO of MIL-100(Fe) and bound to the holes. This demonstrated that the composite W4M1 was a Z-scheme heterojunction.

To further verify the Z-scheme heterojunction structure of W4M1, PbO_2 photo-deposition experiments were carried out. It was deemed that Pb^{2+} could be oxidized by h^+ to form PbO_2 precipitates [66]. As shown in Fig. S10, the elemental analysis clearly showed that the Pb elemental was consistent with W element, implying that PbO_2 was deposited on WO_3 after photo-deposition of PbO_2 experiments. The photo-deposition of PbO_2 further affirmed the Z-scheme mechanism described above.

In summary, the mechanism of W4M1 degradation of SMX was shown in Fig. 8. Under visible light irradiation, both MIL-100(Fe) and WO_3 were excited with photogenerated electrons and holes. The electrons on the CB of WO_3 combined with the holes on the HOMO of MIL-

100(Fe), resulting in the accumulation of holes and electrons in the VB of WO_3 and the LUMO of MIL-100(Fe), respectively. The holes could oxidize SMX directly or continue to react to form $\bullet\text{OH}$ to degrade SMX. The electrons reacted with the dissolved oxygen in the water to form $\bullet\text{O}_2^-$ to participate in the SMX degradation process. Moreover, PDS could capture electrons and the Fe(II)/Fe(III) conversion could produce $\bullet\text{SO}_4$ for efficient degradation of SMX. The $\bullet\text{SO}_4$ could also attack targets by conversion to $\bullet\text{OH}$.

3.5. Possible SMX degradation pathway and toxicity assessment

Based on the UPLC-MS results (Fig. S11) and calculated Fukui index (f_k^0) of the SMX molecule [67], the SMX degradation pathways in W4M1/PDS/light system were proposed in Fig. 9. In pathway A, the S—N bond of SMX could directly cleavage and produce P1 and P2. Then, P2 was transformed into P3 and P4. In pathway B, the hydrogen atom of arylamine in SMX undergo nucleophilic substitution to form P5. Then, cleavage of S—N bond of P5 generated P6. In pathway C, reactive site N8 of SMX was oxidated and formed a classical oxidative product P8. P9 was the result of the direct denigration of P8. Afterward, an attack on C4-S7 bond of P9 led to the creation of P10. The aniline group also might lead to the oxidative formation of product P7 (Pathway D). Finally, the intermediates were able to be further decomposed and mineralized into CO_2 , H_2O , NO_3^- and NH_4^+ .

The toxicity of the formed intermediates could be evaluated by Toxicity Estimation Software (T.E.S.T.), including mutagenicity, developmental toxicity and bioaccumulation factor [8]. Fig. S12a suggested that the mutagenicity of intermediates (except P2) maintained

mutagenicity negative. Moreover, most of the intermediates for developmental toxicity (Fig. S12b) and bioaccumulation factor (Fig. S12c) declined. Thus, the W4M1/PDS/light system would decrease concentration and toxicity of the SMX.

3.6. Recyclability and stability

The performance and structure of materials are critical for their recycling applications. As shown in Fig. 10a, W4M1 synthesized by solvent evaporation method was able to maintain almost 100 % SMX degradation after 5 rounds of cycling, demonstrating that W4M1 had good cycling performance. The leached iron ions concentration in each cycle were shown in Fig. 10b, which were under 0.6 mg/L per round, below the water pollutants standard (2 mg/L) required by the Beijing local standard (DB11/307–2013). The performance stability was related to the structural stability. The TEM and PXRD images of W4M1 after cycling also demonstrated that its structure and morphology did not obviously change (Fig. 10c and 10d). In summary, W4M1 could remain stable during SMX degradation.

4. Conclusion

Series of WO₃/MIL-100(Fe) composites were synthesized by a relatively mild solvent evaporation method and characterized by a range of characterization methods. The SR-AOP performance of the W4M1 was significantly better than that of the pure WO₃ and MIL-100(Fe) due to formation of Z-scheme heterojunction. Under the optimal conditions, the W4M1 degraded ca. 100 % of 5 mg/L SMX within 15 min. It was found that inorganic anions had little effect on the SR-AOP system and sunlight as light source was very effective in removing the SMX. The main active substances of SMX degradation over W4M1 were evidenced by capture experiments. The W4M1 remained almost unchanged after 5 cycles, demonstrating the stability and practical application value.

CRediT authorship contribution statement

Ke-Xin Shi: Data curation, Investigation, Visualization, Software, Writing – original draft. **Fuguo Qiu:** Resources, Validation. **Jia-Wei Wang:** Data curation, Investigation, Visualization, Software. **Peng Wang:** Resources. **Hai-Yan Li:** Resources. **Chong-Chen Wang:** Conceptualization, Funding acquisition, Supervision, Project administration, Writing – review & editing.

Declaration of Competing Interest

The authors declare that they have no known competing financial interests or personal relationships that could have appeared to influence the work reported in this paper.

Data availability

Data will be made available on request.

Acknowledgements

This work was supported by Beijing Natural Science Foundation (8202016), the Pyramid Talent Training Project of Beijing University of Civil Engineering and Architecture (JDLJ20220802, JDYC20220817) and BUCEA Post Graduate Innovation Project (PG2022057).

Appendix A. Supplementary data

Supplementary data to this article can be found online at <https://doi.org/10.1016/j.seppur.2022.122991>.

References

- [1] M.N. Alekshun, S.B. Levy, Molecular mechanisms of antibacterial multidrug resistance, *Cell* 128 (2007) 1037–1050, <https://doi.org/10.1016/j.cell.2007.03.004>.
- [2] Y. Luo, D.Q. Mao, M. Rysz, D.X. Zhou, H.J. Zhang, L. Xu, P.J.J. Alvarez, Trends in Antibiotic Resistance Genes Occurrence in the Haihe River, China, *Environ. Sci. Technol.* 44 (2010) 7220–7225, <https://doi.org/10.1021/es100233w>.
- [3] A.L. Batt, D.D. Snow, D.S. Aga, Occurrence of sulfonamide antimicrobials in private water wells in Washington County, Idaho, USA, *Chemosphere* 64 (2006) 1963–1971, <https://doi.org/10.1016/j.chemosphere.2006.01.029>.
- [4] M.J. Garcia-Galan, S. Gonzalez Blanco, R. Lopez Roldan, S. Diaz-Cruz, D. Barcelo, Ecotoxicity evaluation and removal of sulfonamides and their acetylated metabolites during conventional wastewater treatment, *Sci. Total Environ.* 437 (2012) 403–412, <https://doi.org/10.1016/j.scitotenv.2012.08.038>.
- [5] W. Zhu, F. Sun, R. Goei, Y. Zhou, Facile fabrication of RGO-WO₃ composites for effective visible light photocatalytic degradation of sulfamethoxazole, *Appl. Catal. B: Environ.* 207 (2017) 93–102, <https://doi.org/10.1016/j.apcatb.2017.02.012>.
- [6] H.-Y. Chu, T.-Y. Wang, C.-C. Wang, Advanced Oxidation Processes (AOPs) for Bacteria Removal over MOFs-Based Materials, *Prog. Chem.* in press, <http://doi.org/10.7536/220501>.
- [7] X.-H. Yi, C.-C. Wang, Elimination of emerging organic contaminants in wastewater by advanced oxidation process over iron-based MOFs and their composites, *Prog. Chem.* 33 (2021) 471–489, <https://doi.org/10.7536/PC200562>.
- [8] F.-X. Wang, C.-C. Wang, X. Du, Y. Li, F. Wang, P. Wang, Efficient removal of emerging organic contaminants via photo-Fenton process over micron-sized Fe-MOF sheet, *Chem. Eng. J.* 429 (2022), 132495, <https://doi.org/10.1016/j.cej.2021.132495>.
- [9] J. Lee, U. von Gunten, J.H. Kim, Persulfate-Based Advanced Oxidation: Critical Assessment of Opportunities and Roadblocks, *Environ. Sci. Technol.* 54 (2020) 3064–3081, <https://doi.org/10.1021/acs.est.9b07082>.
- [10] X.-H. Yi, T.-Y. Wang, H.-Y. Chu, Y. Gao, C.-C. Wang, Y.-J. Li, L. Chen, P. Wang, H. Fu, C. Zhao, W. Liu, Effective elimination of tetracycline antibiotics via photoactivated SR-AOP over vivianite: A new application approach of phosphorus recovery product from WWTP, *Chem. Eng. J.* 449 (2022), 137784, <https://doi.org/10.1016/j.cej.2022.137784>.
- [11] X. Li, B. Wang, Y. Cao, S. Zhao, H. Wang, X. Feng, J. Zhou, X. Ma, Water Contaminant Elimination Based on Metal-Organic Frameworks and Perspective on Their Industrial Applications, *ACS Sustain. Chem. Eng.* 7 (2019) 4548–4563, <https://doi.org/10.1021/acssuschemeng.8b05751>.
- [12] Y. Fu, K. Zhang, Y. Zhang, Y. Cong, Q. Wang, Fabrication of visible-light-active MR/NH₂-MIL-125(Ti) homojunction with boosted photocatalytic performance, *Chem. Eng. J.* 412 (2021), 128722, <https://doi.org/10.1016/j.cej.2021.128722>.
- [13] Y.-C. Zhou, P. Wang, H. Fu, C. Zhao, C.-C. Wang, Ternary Ag/Ag₃PO₄/MIL-125-NH₂ Z-scheme heterojunction for boosted photocatalytic Cr(VI) cleanup under visible light, *Chin. Chem. Lett.* 31 (2020) 2645–2650, <https://doi.org/10.1016/j.ccl.2020.02.048>.
- [14] C.-Y. Wang, L. Ma, C.-C. Wang, P. Wang, L. Gutierrez, W. Zheng, Light-response adsorption and desorption behaviors of metal-organic frameworks, *Environ. Funct. Mater.* 1 (2022) 49–66, <https://doi.org/10.1016/j.efmat.2022.05.002>.
- [15] C.-Y. Wang, C.-C. Wang, X.-W. Zhang, X.-Y. Ren, B. Yu, P. Wang, Z.-X. Zhao, H. Fu, A new Eu-MOF for ratiometrically fluorescent detection toward quinolone antibiotics and selective detection toward tetracycline antibiotics, *Chin. Chem. Lett.* 33 (2022) 1353–1357, <https://doi.org/10.1016/j.ccl.2021.08.095>.
- [16] Y.-H. Li, P. Wang, C.-C. Wang, L. y.b., State-Of-The-Art Review of Defective Metal-Organic Frameworks for Pollutant Removal from Water, *Chin. J. Inorg. Chem.* 38 (2022), <https://doi.org/10.11862/CJIC.2022.252>.
- [17] H. Fu, Z. Feng, S.-S. Liu, P. Wang, C. Zhao, C.-C. Wang, Enhanced ethanol sensing performance of N-doped ZnO derived from ZIF-8, *Chin. Chem. Lett.* (2022), <https://doi.org/10.1016/j.ccl.2022.04.023>.
- [18] Y.-H. Li, C.-C. Wang, X. Zeng, X.-Z. Sun, C. Zhao, H. Fu, P. Wang, Seignette salt induced defects in Zr-MOFs for boosted Pb(II) adsorption: universal strategy and mechanism insight, *Chem. Eng. J.* 442 (2022), <https://doi.org/10.1016/j.cej.2022.136276>.
- [19] C. Zhao, J. Wang, X. Chen, Z. Wang, H. Ji, L. Chen, W. Liu, C.C. Wang, Bifunctional Bi₁₂O₁₇Cl₂/MIL-100(Fe) composites toward photocatalytic Cr(VI) sequestration and activation of persulfate for bisphenol A degradation, *Sci. Total Environ.* 752 (2021), 141901, <https://doi.org/10.1016/j.scitotenv.2020.141901>.
- [20] J. Zhou, X. An, Q. Tang, H. Lan, Q. Chen, H. Liu, J. Qu, Dual channel construction of WO₃ photocatalysts by solution plasma for the persulfate-enhanced photodegradation of bisphenol A, *Appl. Catal. B: Environ.* 277 (2020), 119221, <https://doi.org/10.1016/j.apcatb.2020.119221>.
- [21] H. Ding, J. Hu, Enhancing the degradation of carbamazepine by UVA-LED/WO₃ process with peroxydisulfate: Effects of light wavelength and water matrix,

- J. Hazard. Mater. 404 (2021), 124126, <https://doi.org/10.1016/j.jhazmat.2020.124126>.
- [22] H. Yang, Z.-C. Zhao, Y.-P. Yang, Z. Zhang, W. Chen, R.-Q. Yan, Y. Jin, J. Zhang, Defective WO₃ nanoplates controllably decorated with MIL-101(Fe) nanoparticles to efficiently remove tetracycline hydrochloride by S-scheme mechanism, Sep. Purif. Technol. 300 (2022), 121846, <https://doi.org/10.1016/j.seppur.2022.121846>.
- [23] J.-W. Wang, F.-G. Qiu, P. Wang, C. Ge, C.-C. Wang, Boosted bisphenol A and Cr(VI) cleanup over Z-scheme WO₃/MIL-100(Fe) composites under visible light, J. Clean. Prod. 279 (2021), <https://doi.org/10.1016/j.jclepro.2020.123408>.
- [24] S. Zhang, S. Chen, D. Liu, J. Zhang, T. Peng, Layered WS₂/WO₃ Z-scheme photocatalyst constructed via an in situ sulfurization of hydrous WO₃ nanoplates for efficient H₂ generation, Appl. Surf. Sci. 529 (2020), 147013, <https://doi.org/10.1016/j.apsusc.2020.147013>.
- [25] L. Wu, C.C. Wang, H.Y. Chu, X.H. Yi, P. Wang, C. Zhao, H. Fu, Bisphenol A cleanup over MIL-100(Fe)/CoS composites: Pivotal role of Fe-S bond in regenerating Fe²⁺ ions for boosted degradation performance, Chemosphere 280 (2021), 130659, <https://doi.org/10.1016/j.chemosphere.2021.130659>.
- [26] Y.P. Xie, G. Liu, L. Yin, H.-M. Cheng, Crystal facet-dependent photocatalytic oxidation and reduction reactivity of monoclinic WO₃ for solar energy conversion, J. Mater. Chem. 22 (2012) 6746, <https://doi.org/10.1039/c2jm16178h>.
- [27] Y. Li, Z. Tang, J. Zhang, Z. Zhang, Exposed facet and crystal phase tuning of hierarchical tungsten oxide nanostructures and their enhanced visible-light-driven photocatalytic performance, CrystEngComm 17 (2015) 9102–9110, <https://doi.org/10.1039/c5ce01829c>.
- [28] X. Wang, H. Fan, P. Ren, Effects of exposed facets on photocatalytic properties of WO₃, Adv. Powder Technol. 28 (2017) 2549–2555, <https://doi.org/10.1016/j.appt.2017.07.005>.
- [29] Y. Li, Z. Tang, J. Zhang, Z. Zhang, Enhanced photocatalytic performance of tungsten oxide through tuning exposed facets and introducing oxygen vacancies, J. Alloy. Compd. 708 (2017) 358–366, <https://doi.org/10.1016/j.jallcom.2017.03.046>.
- [30] N. Zhang, C. Chen, Z. Mei, X. Liu, X. Qu, Y. Li, S. Li, W. Qi, Y. Zhang, J. Ye, V. A. Roy, R. Ma, Monoclinic Tungsten Oxide with 100 Facet Orientation and Tuned Electronic Band Structure for Enhanced Photocatalytic Oxidations, ACS Appl. Mater. Inter. 8 (2016) 10367–10374, <https://doi.org/10.1021/acsami.6b02275>.
- [31] B. Xu, Z. Chen, B. Han, C. Li, Glycol assisted synthesis of MIL-100(Fe) nanospheres for photocatalytic oxidation of benzene to phenol, Catal. Commun. 98 (2017) 112–115, <https://doi.org/10.1016/j.catcom.2017.04.041>.
- [32] R. Liang, S. Luo, F. Jing, L. Shen, N. Qin, L. Wu, A simple strategy for fabrication of Pd@MIL-100(Fe) nanocomposite as a visible-light-driven photocatalyst for the treatment of pharmaceuticals and personal care products (PPCPs), Appl. Catal. B: Environ. 176–177 (2015) 240–248, <https://doi.org/10.1016/j.apcatb.2015.04.009>.
- [33] N.M. Mahmoodi, J. Abdi, M. Oveis, M. Alinia Asli, M. Vossoughi, Metal-organic framework (MIL-100 (Fe)): Synthesis, detailed photocatalytic dye degradation ability in colored textile wastewater and recycling, Mater. Res. Bull. 100 (2018) 357–366, <https://doi.org/10.1016/j.materresbull.2017.12.033>.
- [34] L. Chen, X. Wang, Z. Rao, Z. Tang, Y. Wang, G. Shi, G. Lu, X. Xie, D. Chen, J. Sun, In-situ synthesis of Z-scheme MIL-100(Fe)/ α -Fe₂O₃ heterojunction for enhanced adsorption and Visible-light photocatalytic oxidation of O-xylene, Chem. Eng. J. 416 (2021), 129112, <https://doi.org/10.1016/j.cej.2021.129112>.
- [35] J. Fu, Q. Xu, J. Low, C. Jiang, J. Yu, Ultrathin 2D/2D WO₃/g-C₃N₄ step-scheme H₂-production photocatalyst, Appl. Catal. B: Environ. 243 (2019) 556–565, <https://doi.org/10.1016/j.apcatb.2018.11.011>.
- [36] C. Yang, Y. Zhu, J. Wang, W. Sun, L. Yang, H. Lin, S. Lv, A novel granular MOF composite with dense and ordered MIL-100(Fe) nanoparticles grown on porous alumina: Green synthesis and enhanced adsorption of tetracycline hydrochloride, Chem. Eng. J. 426 (2021), 131724, <https://doi.org/10.1016/j.cej.2021.131724>.
- [37] M. Tang, Y. Ao, P. Wang, C. Wang, All-solid-state Z-scheme WO₃ nanorod/ZnIn₂S₄ composite photocatalysts for the effective degradation of nitenpyram under visible light irradiation, J. Hazard. Mater. 387 (2020), 121713, <https://doi.org/10.1016/j.jhazmat.2019.121713>.
- [38] K.-X. Shi, F. Qiu, P. Wang, H. Li, C.-C. Wang, Magnetic MgFe₂O₄/MIL-88A catalyst for photo-Fenton sulfamethoxazole decomposition under visible light, Sep. Purif. Technol. 301 (2022), <https://doi.org/10.1016/j.seppur.2022.121965>.
- [39] R. Wang, G. Qiu, Y. Xiao, X. Tao, W. Peng, B. Li, Optimal construction of WO₃-H₂O/Pd/CdS ternary Z-scheme photocatalyst with remarkably enhanced performance for oxidative coupling of benzylamines, J. Catal. 374 (2019) 378–390, <https://doi.org/10.1016/j.jcat.2019.05.016>.
- [40] W. Liu, Q. Kang, L. Wang, L. Wen, Z. Li, Facile synthesis of Z-scheme g-C₃N₄@MIL-100 (Fe) and the efficient photocatalytic degradation on doxycycline and disinfection by-products by coupling with persulfate: Mechanism and pathway, Colloids Surf., A 635 (2022), 128057, <https://doi.org/10.1016/j.colsurfa.2021.128057>.
- [41] H. Tian, T. Araya, R. Li, Y. Fang, Y. Huang, Removal of MC-LR using the stable and efficient MIL-100/MIL-53 (Fe) photocatalyst: The effect of coordinate immobilized layers, Appl. Catal. B: Environ. 254 (2019) 371–379, <https://doi.org/10.1016/j.apcatb.2019.04.086>.
- [42] M. Chen, N. Wang, X. Wang, Y. Zhou, L. Zhu, Enhanced degradation of tetrabromobisphenol A by magnetic Fe₃O₄@ZIF-67 composites as a heterogeneous Fenton-like catalyst, Chem. Eng. J. 413 (2021), 127539, <https://doi.org/10.1016/j.cej.2020.127539>.
- [43] L.V.C. Lima, M. Rodriguez, V.A.A. Freitas, T.E. Souza, A.E.H. Machado, A.O. T. Patrocínio, J.D. Fabris, L.C.A. Oliveira, M.C. Pereira, Synergism between n-type WO₃ and p-type δ -FeOOH semiconductors: High interfacial contacts and enhanced photocatalysis, Appl. Catal. B: Environ. 165 (2015) 579–588, <https://doi.org/10.1016/j.apcatb.2014.10.066>.
- [44] J. Liu, X. Zhang, Q. Zhong, J. Li, H. Wu, B. Zhang, L. Jin, H.B. Tao, B. Liu, Electrostatic self-assembly of a AgI/Bi₂Ga₄O₉ p-n junction photocatalyst for boosting superoxide radical generation, J. Mater. Chem. A 8 (2020) 4083–4090, <https://doi.org/10.1039/c9ta13724f>.
- [45] H. Fu, S. Ma, P. Zhao, S. Xu, S. Zhan, Activation of peroxymonosulfate by graphitized hierarchical porous biochar and MnFe₂O₄ magnetic nanoarchitecture for organic pollutants degradation: Structure dependence and mechanism, Chem. Eng. J. 360 (2019) 157–170, <https://doi.org/10.1016/j.cej.2018.11.207>.
- [46] Y. Qian, J. Huang, J. Chen, G. Xue, Z. Zhou, P. Gao, Activation of peracetic acid by RuO₂/MWCNTs to degrade sulfamethoxazole at neutral condition, Chem. Eng. J. 431 (2022), 134217, <https://doi.org/10.1016/j.cej.2021.134217>.
- [47] H. Li, J. Wan, Y. Ma, Y. Wang, Z. Guan, Role of inorganic ions and dissolved natural organic matters on persulfate oxidation of acid orange 7 with zero-valent iron, RSC Adv. 5 (2015) 99935–99943, <https://doi.org/10.1039/c5ra16094d>.
- [48] L. Hu, P. Wang, G. Liu, Q. Zheng, G. Zhang, Catalytic degradation of p-nitrophenol by magnetically recoverable Fe₃O₄ as a persulfate activator under microwave irradiation, Chemosphere 240 (2020), 124977, <https://doi.org/10.1016/j.chemosphere.2019.124977>.
- [49] W. Zhang, S. Zhou, J. Sun, X. Meng, J. Luo, D. Zhou, J. Crittenden, Impact of Chloride Ions on UV/H₂O₂ and UV/Persulfate Advanced Oxidation Processes, Environ. Sci. Technol. 52 (2018) 7380–7389, <https://doi.org/10.1021/acs.est.8b01662>.
- [50] Y. Yang, J.J. Pignatello, J. Ma, W.A. Mitch, Comparison of halide impacts on the efficiency of contaminant degradation by sulfate and hydroxyl radical-based advanced oxidation processes (AOPs), Environ. Sci. Technol. 48 (2014) 2344–2351, <https://doi.org/10.1021/es404118q>.
- [51] Z. Wu, Y. Wang, Z. Xiong, Z. Ao, S. Pu, G. Yao, B. Lai, Core-shell magnetic Fe₃O₄@Zn/Co-ZIFs to activate peroxymonosulfate for highly efficient degradation of carbamazepine, Appl. Catal. B: Environ. 277 (2020), 119136, <https://doi.org/10.1016/j.apcatb.2020.119136>.
- [52] Y. Zhao, Y. Zhao, Q. Li, R. Zhou, X. Chen, Effect of common inorganic ions on aniline degradation in groundwater by activated persulfate with ferrous iron, Water Supply 16 (2016) 667–674, <https://doi.org/10.2166/ws.2015.174>.
- [53] R. El Asmar, A. Baalbaki, Z. Abou Khalil, S. Naim, A. Bejjani, A. Ghauch, Iron-based metal organic framework MIL-88-A for the degradation of naproxen in water through persulfate activation, Chem. Eng. J. 405 (2021) 125107, <https://doi.org/10.1016/j.cej.2020.126701>.
- [54] Z. Niu, C. Qiu, J. Jiang, L. Ai, Hierarchical CoP–FeP Branched Heterostructures for Highly Efficient Electrocatalytic Water Splitting, ACS Sustain. Chem. Eng. 7 (2019) 2335–2342, <https://doi.org/10.1021/acsschemeng.8b05089>.
- [55] X.-H. Yi, H. Ji, C.-C. Wang, Y. Li, Y.-H. Li, C. Zhao, A. Wang, H. Fu, P. Wang, X. Zhao, W. Liu, Photocatalysis-activated SR-AOP over PDINH/MIL-88A(Fe) composites for boosted chloroquine phosphate degradation: Performance, mechanism, pathway and DFT calculations, Appl. Catal. B: Environ. 293 (2021), 120229, <https://doi.org/10.1016/j.apcatb.2021.120229>.
- [56] I. Ibrahim, A. Kaltzoglou, C. Athanaseou, F. Katsaros, E. Devlin, A.G. Kontos, N. Ioannidis, M. Perraki, P. Tsakiridis, L. Sygellou, M. Antoniadou, P. Palaras, Magnetically separable TiO₂/CoFe₂O₄/Ag nanocomposites for the photocatalytic reduction of hexavalent chromium pollutant under UV and artificial solar light, Chem. Eng. J. 381 (2020), 122730, <https://doi.org/10.1016/j.cej.2019.122730>.
- [57] N. Khoshroshahi, M.D. Goudarzi, M.E. Gilvan, V. Safarifar, Collocation of MnFe₂O₄ and UiO-66(NH₂): An efficient and reusable nanocatalyst for achieving high-performance in hexavalent chromium reduction, J. Mol. Struct. 132994 (2022), <https://doi.org/10.1016/j.jmolstruc.2022.132994>.
- [58] T. Zhou, G. Zhang, H. Zhang, H. Yang, P. Ma, X. Li, X. Qiu, G. Liu, Highly efficient visible-light-driven photocatalytic degradation of rhodamine B by a novel Z-scheme Ag₃PO₄/MIL-101/NiFe₂O₄ composite, Catal. Sci. Technol. 8 (2018) 2402–2416, <https://doi.org/10.1039/c8cy00182k>.
- [59] L.X. Yang, J.E. Yang, M.L. Fu, Magnetic CoFe₂O₄ nanocrystals derived from MIL-101 (Fe/Co) for peroxymonosulfate activation toward degradation of chloramphenicol, Chemosphere 272 (2021), 129567, <https://doi.org/10.1016/j.chemosphere.2021.129567>.
- [60] M. Pu, J. Wan, F. Zhang, M.L. Brusseau, D. Ye, J. Niu, Insight into degradation mechanism of sulfamethoxazole by metal-organic framework derived novel magnetic Fe@C composite activated persulfate, J. Hazard. Mater. 414 (2021), 125598, <https://doi.org/10.1016/j.jhazmat.2021.125598>.
- [61] L. Niu, G. Zhang, G. Xian, Z. Ren, T. Wei, Q. Li, Y. Zhang, Z. Zou, Tetracycline degradation by persulfate activated with magnetic γ -Fe₂O₃/CeO₂ catalyst: Performance, activation mechanism and degradation pathway, Sep. Purif. Technol. 259 (2021), 118156, <https://doi.org/10.1016/j.seppur.2020.118156>.
- [62] L. Zhou, W. Zhang, L. Chen, H. Deng, Z-scheme mechanism of photogenerated carriers for hybrid photocatalyst Ag₃PO₄/g-C₃N₄ in degradation of sulfamethoxazole, J. Colloid Interf. Sci. 487 (2017) 410–417, <https://doi.org/10.1016/j.jcis.2016.10.068>.
- [63] R. Yin, W. Guo, H. Wang, J. Du, Q. Wu, J.-S. Chang, N. Ren, Singlet oxygen-dominated peroxydisulfate activation by sludge-derived biochar for sulfamethoxazole degradation through a nonradical oxidation pathway: Performance and mechanism, Chem. Eng. J. 357 (2019) 589–599, <https://doi.org/10.1016/j.cej.2018.09.184>.
- [64] J. Jiang, X. Wang, Y. Liu, Y. Ma, T. Li, Y. Lin, T. Xie, S. Dong, Photo-Fenton degradation of emerging pollutants over Fe-POM nanoparticle/porous and ultrathin g-C₃N₄ nanosheet with rich nitrogen defect: Degradation mechanism, pathways, and products toxicity assessment, Appl. Catal. B: Environ. 278 (2020), 119349, <https://doi.org/10.1016/j.apcatb.2020.119349>.

- [65] G. Fan, X. Liu, X. Li, C. Lin, M. He, W. Ouyang, Mechanochemical treatment with CaO-activated PDS of HCB contaminated soils, *Chemosphere* 257 (2020), 127207, <https://doi.org/10.1016/j.chemosphere.2020.127207>.
- [66] R. Cao, H. Yang, S. Zhang, X. Xu, Engineering of Z-scheme 2D/3D architectures with Ni(OH)₂ on 3D porous g-C₃N₄ for efficiently photocatalytic H₂ evolution, *Appl. Catal. B: Environ.* 258 (2019), 110903, <https://doi.org/10.1016/j.apcatb.2019.117997>.
- [67] J. Du, W. Guo, H. Wang, R. Yin, H. Zheng, X. Feng, D. Che, N. Ren, Hydroxyl radical dominated degradation of aquatic sulfamethoxazole by Fe⁰/bisulfite/O₂: kinetics, mechanisms, and pathways, *Water Res.* 138 (2018) 323–332, <https://doi.org/10.1016/j.watres.2017.12.046>.